# Engineering Materials

For further volumes:
http://www.springer.com/series/4288

Alexandru Aldea · Victor Bârsan
Editors

# Trends in Nanophysics

## Theory, Experiment and Technology

With 164 Figures and 11 Tables

Springer

*Editors*
Prof. Dr. Alexandru Aldea
National Institute for Materials
Physics (INFM)
Atomistilor St. 105
077125 Magurele-Bucharest
Romania
aldea@infim.ro

Dr. Victor Bârsan
Horia Hulubei National Institute for Physics
and Nuclear Engineering (IFIN-HH)
Atomistilor St. 407
077125 Magurele-Bucharest
Romania
vbarsan@theory.nipne.ro

ISSN 1612-1317 e-ISSN 1868-1212
ISBN 978-3-642-12069-5 e-ISBN 978-3-642-12070-1
DOI 10.1007/978-3-642-12070-1
Springer Heidelberg Dordrecht London New York

Library of Congress Control Number: 2010927488



*Cover design*: deblik, Berlin

Printed on acid-free paper

Springer is part of Springer Science+Business Media (www.springer.com)

# Preface

This volume is based on some representative contributions presented in the workshop: "Trends in nanophysics: theory, experiment, technology", which took place in Sibiu, Romania, 23–29 August 2009, being organized by ICTP-Trieste, IAEA, IFIN-HH – Bucharest and ULB – Sibiu. The aim of this workshop was to facilitate experts and active researchers to exchange ideas and information on the most recent results in nanophysics and nanotechnology. It was also an opportunity for young researchers and for researchers from developing countries to enlarge their knowledge and to approach new themes in this area.

In fact, the articles contained in this book represent written and enriched versions of the workshop oral presentations. The topics covered by them are the following:

1. Ordered atomic-scale structures
2. Nanowires: growth and properties
3. Transport phenomena in nanostructures
4. Optical properties of nanostructures
5. Magnetic nanophases; magnetic and non-magnetic nanocomposites
6. Nanofluids and flows at nanoscale

## 1 Ordered Atomic-Scale Structures

The quest of a reliable method for fabricating ordered atomic-scale structures is a prerequisite for future atomic-scale technology – the ultimate goal of nanosciences. In his lecture devoted to this subject, Schneider reviews selected examples concerning atomic and supra-molecular self-assembly investigated by low temperature scanning tunneling microscopy: two-dimensional arrays of individual Ce atoms on a metal surface; the behaviour of the superconductor energy gap in ultra-thin Pb islands and the conservation of chirality in a hierarchical supra-molecular self-assembly of pentagonal symmetry of rubene on an Au surface. Another key issue for the success of many nanotechnologies is our ability to understand the mechanics of nano-objects, such as nanotubes and nanobelts. Dumitrica's contribution is devoted to an ingenious symmetry-adapted atomistic scheme, based on a quantum-mechanical description of chemical bonding, that performs calculations under

helical boundary conditions. As an application, the nanomechanical response of carbon nanotubes and thermodynamical stability of silicon nanowires are obtained.

## 2 Nanowires: Growth and Properties

Growths and properties of nanowires are a central issue of nanoscience and nanotechnology. Lakhtakis's paper presents a new class of assemblies of nanowires, named sculptured thin films, that can be fabricated typically via physical vapor deposition onto rotating substrates. Their optical properties can be tailored by varying their morphology. The optical, thermal, chemical, and biological applications of sculptured thin films are reviewed. Stoica's contribution is focused on growths and optical properties of an important class of semiconductor nanowires – GaN and InN ones, obtained by self-assambling, with a catalist-free molecular beam epitaxy technique. The optoelectronic properties, as well as the influence of surface effects on the growth and properties of these nanowires are carefully analyzed.

## 3 Transport Phenomena in Nanostructures

The permanent requirement of shrinking the semiconductor devices in integrated circuits request a good understanding of transport phenomena in nanostructures. A comprehensive review of such topics is given in the presentation of Kuhn and Paraoanu, devoted to electronic and thermal sequential transport in metallic and superconducting two-junction arrays. The authors analyse Coulomb-blockade thermometers, superconductor-insulator-normal-insulator-superconductor structures, and superconducting single-electron transistors. Racec et al. present a general theory of multi-channel scattering for a general two-dimensional potential, based on the R-matrix formalism; it allows a semi-analytical treatment of the problem, and yields a powerful and efficient numerical method, with applications to nanostructures with quantum dots. In the review of Nemnes et al., planar nanoscale transistors and cylindrical nanowire transistors are analyzed in the framework of coherent transport. The Landauer-Buttiker formalism is efficiently implemented using also a R-matrix approach. The advantages of new geometries, like the cylindrical nanowire transistors, are discussed. As charge fractionalization has been observed experimentally in quantum wires, this fundamental phenomenon deserves special attention. In his lecture, Leinaas discusses the issue of fractional charge and statistics in Luttinger liquids – one of the most popular models describing one-dimensional systems of fermions.

## 4 Optical Properties of Nanostructures

If trapping and moving of dielectric nanoparticles with laser beams constitute a well understood issue, the situation of metallic nanoparticle is quite different. In Prof. Crozier's contribution, it is explained how the propulsion of gold nanoparticles by

surface plasmon polaritons was demonstrated experimentally. The optical forces are enhanced, due to the field enhancement provided by plasmon polaritons and near-field coupling between the gold particle and the film. The plasmon spectra of plasmons excited in metallic nanoparticles and nanowires are discussed also in a theoretical paper, by Villo-Perez, Mišković, and Arista. They apply Bloch's hydrodynamic model of an electron gas to describe plasma excitations in thin metallic films, obtaining a good description of the excitation, propagation and decay of bulk and surface modes, in different geometries. A two-fluid model, in which the $\sigma$ and $\pi$ electrons of carbon are the constituents of these fluids, is used in order to obtain the plasmon spectra in carbon nanotubes.

## 5 Magnetic Nanophases; Magnetic and Non-Magnetic Nanocomposites

Nanomagnetism is important for both fundamental and applicative reasons. Functionalized nanocomposites consisting of magnetic nanoparticles (Co, Fe), embedded in dielectric matrices, have a significant potential for the electronics industry. In the contribution of Timonen et al., the theory of such materials is reviewed; also, the authors present a novel measurement method used for the characterization of the electromagnetic properties of composites with nano-magnetic insertions. The article of Tolea et al. is devoted to spring magnets, consisting of interfaced hard (containing rare earths, iron and boron) and soft (containing iron and boron) magnetic nanophases, coupled by exchange interactions. Their magnetic properties depend on the thermal treatment and of amount of added iron, the optimal situation corresponding when hard and soft magnetic phases coexist with a small amorphous phase. Kuncser et al. describe how Mossbauer spectroscopy, applyed in complementarity with magnetic and structural techniques, can be used in order to obtain a comprehensive characterization of the magnetic configuration and magnetic relaxation of nanoparticles. The contribution of Jovanovic et al. is devoted to non-magnetic nanocomposites: silver nanoparticles embedded in a hydrogel, synthetized in situ by gamma iradiation. The plasmon spectra of nanoparticles are described and the biomedical applications are discussed.

## 6 Nanofluids and Flows at Nanoscale

The characterization of nanofluids, consisting of dispersed magnetic nanoparticles in a liquid carrier, is important mainly due to the the specific applications of such complex magnetic systems. Prof. Chicea's contribution is focused on magnetite nanoparticle aggregation dynamics in an aqueous suspension and on its effects on the modification of the rheological properties of the fluid.The time variation of the average diameter of the aggregates is obtained using light scattering techniques. Last but not the least, Prof. Niemela's contribution reviews some of the nano-physics appearing in the turbulent flow of classical and quantum fluids.

We hope that the diversity of themes and the clarity of contributions, written by leading experimental and theoretical researchers in these fields, recommend this volume as a useful and attractive lecture for researchers or students interested in nanophysics.

Bucharest, Romania

Alexandru Aldea
Victor Bârsan

# Acknowledgements

The editors are grateful to EOARD and ANCS for their financial support, which was essential for the organization of the workshop. They are also grateful to Springer Publishing House, for its interest in the publication of these proceedings.

Bucharest, Romania

Alexandru Aldea
Victor Bârsan

# Contents

# Contributors

**R. Alexandrescu** National Institute for Lasers, Plasma and Radiation Physics (INFLPR), 409 Atomistilor St., 077125 Bucharest-Magurele, Romania, ralexandrescu2001@yahoo.co.uk

**S. Antohe** Faculty of Physics, University of Bucharest, "Materials and Devices for Electronics and Optoelectronics" Research Center, PO Box MG-11, 077125 Magurele-Ilfov, Romania, santohe@solid.fizica.unibuc.ro

**N.R. Arista** División Colisiones Atómicas, Instituto Balseiro and Centro Atómico Bariloche, Comisión Nacional de Energía Atómica, 8400 Bariloche, Argentina, arista001@yahoo.com

**A. Birsan** National Institute of Materials Physics (INFM), 105 Atomistilor Street, 077125 Magurele-Bucharest, Romania, ancutabirsan@yahoo.com

**Raffaella Calarco** Institute of Bio- and Nanosystems (IBN-1) and JARA-FIT Jülich-Aachen Research Alliance, Forschungszentrum Jülich, 52425 Jülich, Germany, R.Calarco@fz-juelich.de

**Khattiya Chalapat** Low Temperature Laboratory, School of Science and Technology, Aalto University, PO Box 15100, FI-00076 Aalto, Finland, khattiya.chalapat@ltl.tkk.fi

**Dan Chicea** Department of Physics, University Lucian Blaga of Sibiu, Dr. Ion Ratiu Str. 7-9, Sibiu 550012 Romania, dan.chicea@ulbsibiu.ro

**Kenneth B. Crozier** School of Engineering and Applied Science, Harvard University, Cambridge, MA 02138, USA, kcrozier@seas.harvard.edu

**M. Dragašević** Institute of Endocrinology, Diabetes and Metabolic Diseases, University Clinical Centre of Serbia, Dr Subotića 13, 1100 Belgrade, Serbia, mirdraga@yahoo.com

**Traian Dumitrica** Department of Mechanical Engineering, University of Minnesota, Minneapolis, MN, USA, td@me.umn.edu

**G. Filoti** National Institute for Materials Physics (INFM), 105 Atomistilor Street, 077125 Magurele-Bucharest, Romania, filoti@infim.ro

**Joseph B. Geddes III** Beckman Institute, University of Illinois at Urbana–Champaign, Urbana, IL 61801, USA, jbgeddes3@jbg3.net

**Olli Ikkala** Molecular Materials, Department of Applied Physics, School of Science and Technology, Aalto University, PO Box 15100, FI-00076 Aalto, Finland, Olli.Ikkala@tkk.fi

**L. Ion** Faculty of Physics, University of Bucharest, "Materials and Devices for Electronics and Optoelectronics" Research Center, PO Box MG-11, 077125 Magurele-Ilfov, Romania

**Ž. Jovanović** Faculty of Technology and Metallurgy, University of Belgrade, PO Box 3503, 11120 Belgrade, Serbia, zjovanovic@tmf.bg.ac.rs

**Z. Kačarević-Popović** Vinča Institute of Nuclear Sciences, University of Belgrade, PO Box 522, 11001 Belgrade, Serbia, zkacar@vinca.rs

**A. Krklješ** Vinca Institute of Nuclear Sciences, University of Belgrade, PO Box 522, 11001 Belgrade, Serbia, krkljes@vinca.rs

**T. Kühn** NanoScience Center and Department of Physics, University of Jyväskylä, Jyväskylä PO Box 35 (YFL), FIN-40014, Finland, kuehn@cc.jyu.fi

**V. Kuncser** National Institute for Materials Physics (INFM), 105 Atomistilor Street, 077125 Magurele-Bucharest, Romania, kuncser@infim.ro

**Akhlesh Lakhtakia** Department of Engineering Science and Mechanics, Pennsylvania State University, University Park, PA 16802, USA, axl4@psu.edu

**Jon Magne Leinaas** Department of Physics, University of Oslo, N-0316 Oslo, Norway, j.m.leinaas@fys.uio.no

**Jian Li** Low Temperature Laboratory, School of Science and Technology, Aalto University, PO Box 15100, FI-00076 Aalto, Finland, jianli@ltl.tkk.fi

**Z.L. Mišković** Department of Applied Mathematics, University of Waterloo, Waterloo, ON, Canada, N2L 3G1, zmiskovic03@gmail.com

**V. Mišković-Stanković** Faculty of Technology and Metallurgy, University of Belgrade, PO Box 3503, 11120 Belgrade, Serbia, vesna@tmf.bg.ac.rs

**I. Morjan** National Institute for Lasers, Plasma and Radiation Physics (INFLPR), 409 Atomistilor St., 077125 Magurele-Bucuresti, Romania, Ion.Morjan@inflpr.ro

**H. Neidhardt** Weierstraß-Institut für Angewandte Analysis und Stochastik, Mohrenstr. 39, 10117 Berlin, Germany, neidhard@wias-berlin.de

**G.A. Nemnes** Faculty of Physics, University of Bucharest, "Materials and Devices for Electronics and Optoelectronics" Research Center, PO Box MG-11, 077125 Magurele-Ilfov, Romania, nemnes@solid.fizica.unibuc.ro

**J.J. Niemela** The Abdus Salam ICTP, Strada Costiera 11, 34014 Trieste, Italy, niemela@ictp.it

**Markku Oksanen** Nokia Research Center, Itämerenkatu 11-13, 00180 Helsinki, Finland, markku.a.oksanen@nokia.com

**G.S. Paraoanu** Low Temperature Laboratory, School of Science and Technology, Aalto University, PO Box 15100, FI-00076 Aalto, Finland, paraoanu@cc.hut.fi

**S. Popović** Institute of Endocrinology, Diabetes and Metabolic Diseases, University Clinical Centre of Serbia, Dr Subotića 13, 1100 Belgrade, Serbia, prof.srdjan.popovic@gmail.com

**E.R. Racec** Institut für Physik, Technische Universität Cottbus, Postfach 101344, 03013 Cottbus, Germany; Faculty of Physics, University of Bucharest, PO Box MG-11, 077125 Bucharest Magurele, Romania, roxana@physik.tu-cottbus.de

**P.N. Racec** Weierstraß-Institut für Angewandte Analysis und Stochastik, Mohrenstr. 39, 10117 Berlin, Germany; National Institute of Materials Physics, PO Box MG-7, 077125 Bucharest Magurele, Romania, racec@wias-berlin.de

**Robin H.A. Ras** Molecular Materials, Department of Applied Physics, School of Science and Technology, Aalto University, PO Box 15100, FI-00076 Aalto, Finland, Robin.Ras@tkk.fi

**G. Schinteie** National Institute of Materials Physics (INFM), 105 Atomistilor Street, 077125 Magurele-Bucharest, Romania, schinteie@infim.ro

**Wolf-Dieter Schneider** Ecole Polytechnique Fédérale de Lausanne (EPFL), Institut de Physique de la Matière Condensée, CH-1015 Lausanne, Switzerland, wolf-dieter.schneider@epfl.ch

**Eira Seppälä** Nokia Research Center, Itämerenkatu 11-13, 00180 Helsinki, Finland, Eira.Seppala@nokia.com

**M. Sofronie** National Institute of Materials Physics (INFM), 105 Atomistilor Street, 077125 Magurele-Bucharest, Romania, sofmiha@yahoo.com

**Toma Stoica** Institute of Bio- and Nanosystems (IBN-1) and JARA-FIT Jülich-Aachen Research Alliance, Forschungszentrum Jülich, 52425 Jülich, Germany, t.stoica@fz-juelich.de

**Eli Sutter** Brookhaven National Laboratory, Center for Functional Nanomaterials, Upton, NY 11973, USA, esutter@bnl.gov

**Jaakko V.I. Timonen** Molecular Materials, Department of Applied Physics, School of Science and Technology, Aalto University, PO Box 15100, FI-00076 Aalto, Finland, jaakko.timonen@tkk.fi

**F. Tolea** National Institute of Materials Physics (INFM), 105 Atomistilor Street, 077125 Magurele-Bucharest, Romania, felicia@infim.ro

**S. Tomić** Faculty of Technology and Metallurgy, University of Belgrade, PO Box 3503, 11120 Belgrade, Serbia, simonida@tmf.bg.ac.rs

**M. Valeanu** National Institute of Materials Physics (INFM), Bucharest-Magurele, Romania, valeanu@infim.ro

**L. Vekas** Centre of Fundamental and Advanced Technical Research, Romanian Academy-Timisoara Division, Timisoara, Romania, vekasladislau@yahoo.co

**I. Villo-Perez** Departamento de Electrónica, Universidad Politécnica de Cartagena, E-30202 Cartagena, Spain, isidro.villo@upct.es

**U. Wulf** Technische Universität Cottbus, Fakultät 1, Postfach 101344, 03013 Cottbus, Germany, wulf@physik.tu-cottbus.de

# List of Acronyms

## Institutions

| | |
|---|---|
| ANCS | Autoritatea Nationala pentru Cercetare Stiintifica (National Authority for Scientific Research) |
| EOARD | European Office for Aerospace Research and Development |
| IAEA | International Agency for Atomic Energy |
| ICTP | International Centre for Theoretical Physics |
| IFIN-HH | Institutul de Fizica si Inginerie Nucleara Horia Hulubei |
| ULB | Universitatea Lucian Blaga |

## Scientific Concepts

| | |
|---|---|
| 2DEG | two-dimensional electron gas |
| AFM | atomic force microscope |
| BCC | body centred cubic |
| BEP | beam-equivalent pressure |
| CBT | Coulomb-blocade thermometer |
| CCD | charge coupled device |
| CNFET | carbon nanotube field-effect transistor |
| CNT | carbon nanotubes |
| DGFET | double gate field-effect transistor |
| DLS | dynamic light scattering |
| DW | domain walls |
| EG | electron gas |
| EMT | effective medium theories |
| FCC | face centred cubic |
| FET | field-effect transistor |
| FMR | ferromagnetic resonance |
| FT | Fourier transformation |
| FWHM | full width at half maximum |
| GAA | gate-all-around |

| | |
|---|---|
| GNR | graphene nano-ribbons |
| HCP | hexagonal close packed |
| HDM | hydrodynamic model |
| HOMO | highest occupied molecular orbital |
| HRTEM | high-resolution transmission electron microscopy |
| IR | infrared |
| kMC | kinetic Monte Carlo |
| KTHNY | Kosterlitz-Thouless-Halperin-Nelson-Young |
| LE | light emission |
| LPS | localized surface plasmon |
| LUMO | lowest unoccupied molecular orbital |
| ML | monolayer |
| MOSFET | metal-oxide-semiconductor field-effect transistor |
| MWCNT | multi-walled CNT |
| NA | numerical aperture |
| NW | nanowire |
| PAMBE | plasma-assisted molecular beam epitaxy |
| PL | photoluminescence |
| PCS | photon correlation spectroscopy |
| PVP | poly(N-vinyl-2-pyrrolidine) |
| RIE | reactive ion etching |
| RKKY | Ruderman-Kittel-Kasuya-Yosida |
| rf | radio frequency |
| RT | room temperature |
| SC | scattering center |
| SD | single-domain |
| SET | single-electron transistor |
| SHF | super high frequency |
| SINIS | superconducting-insulator-normal-insulator-superconducting |
| SLS | static light scattering |
| SNWT | silicon nanowire transistor |
| SOI | silicon-on-insulator |
| SPP | surface plasmon polariton |
| SQUID | Superconducting Quantum Interference Device |
| STM | scanning tunneling microscopy |
| SVP | saturated vapor pressure |
| SWCNT | single-walled CNT |
| TD-DFT | time-dependent density functional theory |
| TE | transversal electric |
| TM | transversal magnetic |
| UHV | ultra-high vacuum |
| vdW | van der Waals |
| VLS | vapor-liquid-solid |
| XRD | X-ray diffraction |

# Part I
# Ordered Atomic-Scale Structures

# Fabrication and Characterization of Ordered Atomic-scale Structures – A Step towards Future Nanoscale Technology

**Wolf-Dieter Schneider**

**Abstract** The quest of a reliable method for fabricating ordered atomic-scale structures is a prequisite for future atomic-scale technology. The interest in such nanostructured materials, consisting of building blocks of a small number of atoms or molecules, arises from their promising new optic, catalytic, magnetic and electronic poperties, which are fundamentally different from their macroscopic bulk counterparts: small is different. Here we review selected examples concerning atomic and supramolecular self-assembly investigated by low-temperature scanning tunneling microscopy (STM). (i) The self-assembly and the melting of a two-dimensional array of individual Ce adatoms (the smallest possible building block) on a metal surface based on long-range interactions between adatoms mediated by surface state electrons. Ce is a magnetic atom, and such hexagonal superlattices of magnetic adatoms might be useful for the development of future atomic-scale magnetic devices. (ii) The reduction of the superconducting energy gap in ultrathin Pb islands grown on Si(111), when the thickness is reduced down to a few atomic with monolayers (MLs). (iii) The conservation of chirality in a hierarchical supramolecular self-assembly of pentagonal symmetry of the organic molecule rubrene on a reconstructed Au(111) surface. We show the spontaneous chiral resolution of the racemate into disjoint homochiral complex architectures and demonstrate the ability to monitor directly the evolution of chiral recognition processes on the molecular and supramolecular level. (iv) Taking advantage of inelastic electron tunneling processes, we excite luminescence from $C_{60}$ and $C_{70}$ molecules in the surface layer of fullerene nanocrystals self-assembled on an ultrathin NaCl film on Au(111). The observed fluorescence and phosphorescence spectra are found to be characteristic for the two molecular species, leading to unambiguous chemical recognition on the molecular scale.

W.-D. Schneider (✉)
Ecole Polytechnique Fédérale de Lausanne (EPFL), Institut de Physique de la Matière Condensée, CH-1015 Lausanne, Switzerland
e-mail: wolf-dieter.schneider@epfl.ch

A. Aldea, V. Bârsan (eds.), *Trends in Nanophysics,* Engineering Materials,
DOI 10.1007/978-3-642-12070-1_1, 

## 1 Introduction

A promising route leading towards the fabrication of ordered nano-scale structures is based on self-assembly of basic building blocks of matter, i.e., of atoms and/or molecules [1]. The key challenges are on one hand, to observe and to characterize the atomic and molecular processes leading to self-assembly and, on the other hand, to determine the electronic and optical properties as well as the chemical identity of the molecular building blocks and of the resulting nanostructures on the molecular level. Here we address both aspects of this challenge employing low-temperature scanning probe techniques. In the first example we present the self-assembly and the melting of 2-D arrays of individual Ce adatoms on Ag(111) and on Cu(111) surfaces, which is based on long-range interactions between adatoms mediated by surface state electrons [2–5]. In the second example we discuss the reduction of the superconducting gap upon the thickness reduction of Pb nano-islands grown on Si(111) [6, 7]. In the third example we discuss the chiral supermolecular self-assembly and the electronic structure of the organic molecule rubrene [8–11], and in the forth example we report on the chemical recognition of $C_{60}$ and $C_{70}$ molecules within the surface layer of self-assembled fullerene nanocrystals by tip-induced fluorescence and phosphorescence [12, 13].

## 2 Experimental

The experiments were performed with a home-built low-temperature ultra-high-vacuum (UHV) STM operating at a pressure of $10^{-11}$ mbar and a temperature of 5 K and of 50 K, using cut PtIr tips. Ce atoms were deposited from a thoroughly degassed tungsten filament onto well prepared Ag(111) and Cu(111) surfaces held at 4.8 K. During specific experiments the temperature of the sample was lowered to 3.0 K by pumping on the He-bath [14].

Pb was thermally evaporated on the Si(111)-7×7 or on the Pb-$\sqrt{3} \times \sqrt{3}$/Si(111) substrate [15] kept at room temperature (RT) favoring the growth of Pb single crystals with their (111) axis perpendicular to the surface [16, 15]. Differential conductance ($dI/dV$) measurements were performed with open feedback loop, using lock-in technique with a modulation voltage of 0.2–0.5 $mV_{pp}$ at $\sim$ 277 Hz, with a typical tunneling current of 1 nA. Radio frequency (rf) noise has been carefully filtered.

The rubrene molecules were deposited at low coverage (0.3 ML) in situ by sublimation from a homebuilt evaporator onto a clean Au(111) substrate at room temperature.

$C_{60}$ and $C_{70}$ nanocrystals were grown on thin insulating NaCl layers deposited onto an atomically flat Au(111) substrate. NaCl was deposited from a resistively heated evaporator onto a clean Au(111) surface at room temperature. Subsequently, the fullerenes were sublimated onto the NaCl covered substrate forming fullerene nanocrystals of hexagonal and truncated triangular shape. Experiments have been

performed at a temperature of 50 K, using etched W tips. Photons emitted from the tunnel junction were collected by a plano-convex lens (NA = 0.34) near the tip-sample gap along the direction 60° with respect to the surface normal. The collected beam was then transmitted through a view port outside the UHV chamber and guided simultaneously to (i) a grating spectrometer (50 l/mm) coupled to a liquid-nitrogen-cooled CCD camera for spectral analysis (90% of the signal) and to (ii) an avalanche photodiode to record the total light intensity and to optimize the alignment of the lens with the tunnel junction (10% of the signal). For the light emission measurements, the tip was positioned over a target location with a fixed tunnel resistance. Spectra were not corrected for the wavelength dependent sensitivity of the detection system. The wavelength resolution of the experiment was 8 nm, corresponding to $\approx 20$ meV in the energy range of interest. The spectra were acquired with closed feedback loop while tunneling over a defined position on the sample, e.g. over a single molecule, with a typical acquisition time of 300 s. Bias voltages $V$ refer to the sample voltage with respect to the tip.

## 3 Results and Discussion

### *3.1 Self-Assembly of Adatom Superlattices*

An interesting possibility to achieve long-range self-assembly of individual atoms with interatomic distances of several lattice constants of the supporting substrate is to take advantage of surface-state-mediated adatom interactions [17] that have been found on noble metal (111) surfaces [18–20]. While the experiments of Refs. [19, 20] displayed preferential adatom-adatom separations illustrating the oscillatory behaviour of the potential of the adatom-adatom interaction mediated by the surface state electrons, no large ordered atomic superlattice was produced. This situation changed when Silly et al. [2, 21] reported on the discovery of the formation of a 2D hexagonal superlattice of Ce adatoms on Ag(111). The control of the temperature permits to tune the adatom mobility on the surface, while the control of the adatom concentration influences the adatom-adatom interaction and, most interestingly, the interatomic distance of the adatoms in the superlattice [2, 3]. The surface state electron scattering at the adatom sites sets the scale of the superlattice constant at a temperature of 4.8 K and a concentration of 1% of a monolayer (ML) of Ce adatoms to 3.2 nm, corresponding closely to half of the Fermi wavelength of the suface state electrons.

Figure 1 shows a STM topograph after deposition of about 1% of a ML of Ce onto Ag(111). The Ce adatoms form a hexagonal superlattice covering the Ag(111) surface. The distance between two neighboring adatoms is determined to be $32 \pm 2$ Å . The superlattice is visible on all large scale STM images but also at different regions of the sample separated by macroscopic distances (2 mm). Such a long-range ordered superlattice was not observed before, neither with Cu on Cu(111) [18, 19] nor with Co adatoms deposited on Ag(111) [20].

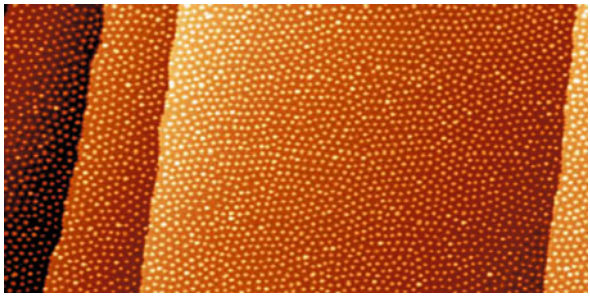

**Fig. 1** 155 × 108 nm$^2$ STM topography of a Ag(111) surface covered by 1% ML of Ce atadoms at a temperature of 3.9 K ($U_s = -90$ mV, $I_s = 40$ pA). Nearest neighbor adatatom-adatom separations are 3.2 nm. Dark (*bright*) contrast: lower (*upper*) terrace separated by a monatomic Ag step. After Ref. [4]

The two-body interaction energy decays as $1/\rho^2$ where $\rho$ is the distance between two adatoms, and oscillates with a period of $\lambda_F/2$, half of the Fermi wavelength of the surface state electrons. A quantitative analysis of the phase shift $\delta_0$ of the surface state electrons scattered at the adatom sites, which can be obtained independently from an analysis of the standing wave patterns, and of the observed adatom mobility around their superlattice sites enabled the determination of the depth of the first minimum in the oscillating two-body interaction potential [22] to 0.8 meV [2, 21].

Thus the self-assembly of the adatom superlattice is a consequence of a subtle balance between the sample temperature, the surface diffusion barrier, and the concentration-dependent adatom interaction potential generated by the surface state electrons. We note that recent kinetic Monte Carlo (kMC) simulations of the self-organisation of Ce adatoms on Ag(111) confirm quantitatively our conclusions [23, 24]. Variation of support and of adatom element as well as adatom concentration may allow us to tune the lattice constant of the superlattice over a wide range [21]. One recent example is the observation of such a superlattice for the adsorption of Cs on Cu(111) where the adatom distance was found to be 1.1 nm, in agreement with the value of half of the Fermi wavelength of the Cu(111) surface state electrons [25, 21].

## *3.2 Melting of Adatom Superlattices*

The first order phase transition which occurs when regular three-dimensional (3D) crystals melt and the highly ordered crystal structure changes into the irregular order of a liquid is well known. In 2D systems, however, melting is fundamentally different. This difference stems from the radical change of the intrinsic properties of matter in reduced dimensions. The long-range order which defines the periodic structure of a 3D crystal changes in 2D to only quasi-long-range translational (or positional) order [26, 27].

According to the Kosterlitz-Thouless-Halperin-Nelson-Young (KTHNY) theory [28–31], a true 2D solid melts in two steps via two distinct successive phase transitions occurring at temperatures $T_m$ and $T_h$, respectively. The intermediate hexatic phase, is thereby characterized by the loss of translational order as for the liquid phase and by the subsistence of a certain degree of orientational order, in contrast to the liquid isotropic phase. For the melting of a 2D solid in the presence of a substrate potential, Nelson and Halperin predicted that the existence of the hexatic phase is hindered and melting directly occurs from the solid into the liquid phase [30].

Many experimental and numerical investigations have been devoted to study the melting transitions in 2D and to verify the KTHNY theory (for a review see [32]) but this new class of atomic 2D superlattices allowed us to directly investigate the melting transition in two dimensions on the atomic scale[5, 21].

For Ce on Ag(111) the adatoms diffuse in the minimum of the superlattice potential already at 4.8 K. Therefore, this system is not well adapted for a detailed melting study because the relatively large adatom-adatom distance and the relatively small interaction energy compared to the diffusion barrier lead to a predicted melting temperature of only $T_m \lesssim 5$ K [5]. Thus, we have examined the temperature evolution of the superlattice of Ce adatoms on Cu(111) [5].

STM images obtained at a temperature of 8 K, 9 K and 14 K, respectively, are shown in Fig. 2a–c. At the elevated temperatures, the Ce adatoms become more mobile on the surface, inducing a modification of the apparent contrast between adatoms and aggregates. The gray-scale insets display the 2D Fourier transformation (FT), corresponding to the structure factor of the positional data. Six sharp and distinct Bragg reflexes, signature of a 2D crystalline order, are observed at 8 K. At 9 K and 14 K the Bragg spots become more diffuse, and a ring appears, indicating melting of the 2D crystal. A weak hexagonal symmetry, however, is still visible in the Fourier transformation even at the elevated temperatures.

In a true 2D system the solid, hexatic, and liquid phases can be identified by a characteristic decay behavior of the pair correlation function $f(r)$, the density-density correlation function $g_r(r)$ and the bond-angular correlation function $g_6(r)$:

$$f(r) = \langle \sum_i \sum_{j \neq i} \delta(r - |\mathbf{r}_i - \mathbf{r}_j|) \rangle \tag{1}$$

$$g_r(|\mathbf{r} - \mathbf{r}'|) = < \exp(i\mathbf{b}[\mathbf{u}(\mathbf{r}) - \mathbf{u}(\mathbf{r}')]) >, \tag{2}$$

$$g_6(|\mathbf{r} - \mathbf{r}'|) = < \exp(i6[\theta(\mathbf{r}) - \theta(\mathbf{r}')]) >, \tag{3}$$

where $\mathbf{b}$ denotes a reciprocal lattice vector of the superlattice, $\mathbf{u}(\mathbf{r})$ is the particle displacement field, $\theta(\mathbf{r})$ is the angle (with respect to a fix axis) of the bond centered at position $\mathbf{r}$. The solid phase is characterized by a quasi-long range positional order and a long range orientational order, corresponding to an algebraic decay of $g_r(r)$ and to the absence of decay of $g_6(r)$ for $r \to \infty$. In the hexatic phase, the positional order is only short range, i. e. decays exponential, while the orientational order is

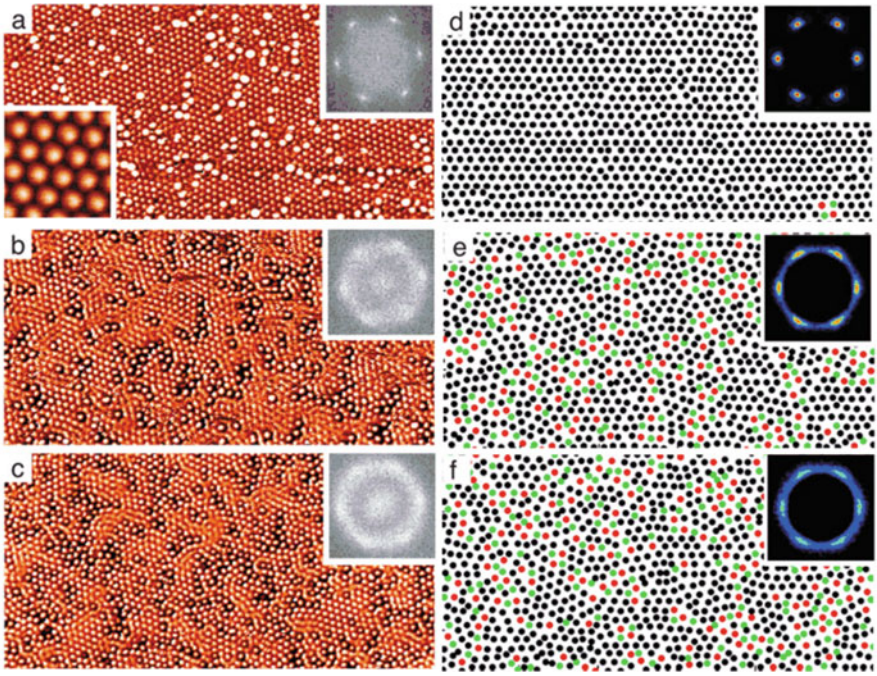


**Fig. 2** (**a**–**c**) STM images ($75 \times 37$ nm$^2$, $V = -20$ mV, $I = 20$ pA) acquired on Ce/Cu(111) for increasing temperatures $T$: (**a**) 8 K; (**b**) 9 K; (c) 14 K. About 0.04 ML of Ce adatoms form a macroscopic-ordered superlattice with an interatomic distance of 1.4 nm, as shown in the color inset to (**a**) ($9.3 \times 9.3$ nm$^2$, $V = +1.8$ V, $I = 20$ pA). The grey-scale insets display the FT of each image. (**d**–**f**) Results of kMC simulations for about 0.04 ML Ce on Cu(111) at (**a**) 9 K; (**b**) 10 K; (**c**) 13 K. Black atoms are sixfold coordinated, red sevenfold, and green fivefold. The insets show the FT of each snapshot (Adapted from [5])

quasi-long range (algebraic decay of $g_6(r)$). Finally, in the liquid phase both order parameters are short range, i. e. $g_r(r)$ and $g_6(r)$ decay exponentially.

The extraction of $g_r(r)$ from the experimental data is difficult because it would require a large number of STM images for each temperature. However, from our data it was possible to compute the pair correlation function. For $T = 8$ K a power-law decay $f(r) \sim r^{-a}$ with $a \approx 0.9$ was found. For $T = 9$ and 14 K we observed an exponential decay, see Fig. 3a. This finding unambiguously shows that at 8 K the system is in the solid phase, while at $T \geq 9$ K the translational order is destroyed. The results for $g_6(r)$, deduced from the STM images of figure 2(a-c) and summarized in Fig. 3(b), reveal that in the solid state at $T = 8$ K, $g_6(r)$ tends to a finite value in agreement with the prediction of the KTNHY theory. The behavior of $g_6(r)$ for 9 and 14 K, however, is not the one expected for a true 2D system: $g_6(r)$ approaches a constant value for large $r$, and does not decay to zero despite the fact that the translational order is destroyed.

An extensive theoretical investigation has been performed to clarify the 2D melting process for the Ce superlattice on Cu(111) [5]. The long-range interaction

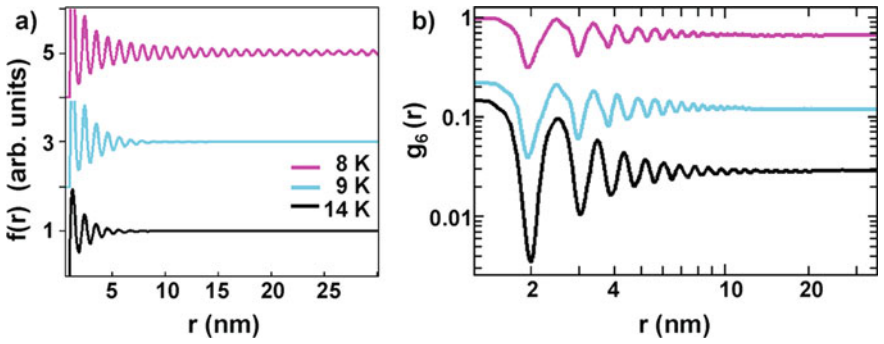


**Fig. 3** (**a**) Pair correlation function $f(r)$ and (**b**) bond-angular correlation function $g_6(r)$ extracted from the experimental data shown in figure 2(a-c) (Adapted from [5])

between two single Ce adatoms at different interatomic separations was deduced using ab initio density functional theory. This calculated long-range interaction potential was then used in a large-scale kinetic Monte-Carlo simulation [5] in which the surface was represented by a triangular lattice of equivalent fcc and hcp hollow sites.

The results obtained for different temperatures are presented in Fig. 2d–f. For $T = 8$ K a 2D ordered solid is formed by the Ce adatoms, as confirmed by the Fourier transformation in the inset. Almost all atoms are found to be sixfold coordinated (black color code). In the snapshots at elevated temperatures (Fig. 2e, f), the number of adatoms with six nearest neighbors decreases, while the amount of sevenfold (red) and fivefold (green) coordinated atoms increases. In the Fourier transformation of the images a ring appears, indicating that a melting transition has taken place. However, the hexagonal symmetry persists, with a striking resemblance to the experimental data of Fig. 2a–c.

Figure 4a shows the density-density correlation function $g_r(r)$ obtained for the Ce/Cu(111) kinetic Monte Carlo simulations at different temperatures. At temperatures $T \leq 9$ K, the system exhibits crystalline long-range order, as seen in

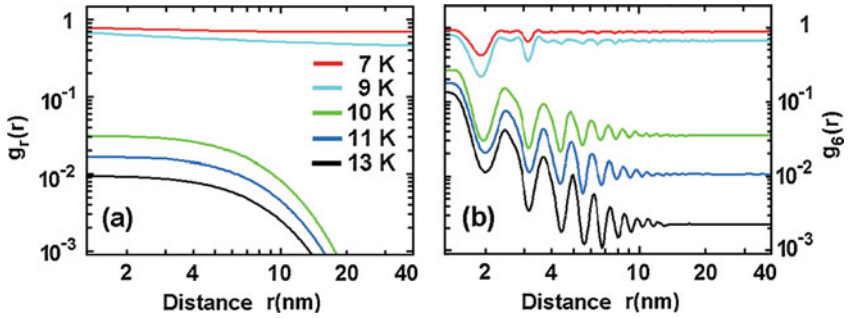


**Fig. 4** (**a**) Density-density $g_r(r)$, (**b**) bond-angular $g_6(r)$ correlation functions calculated for about 0.04 ML of Ce on Cu(111) generated by kinetic Monte Carlo simulations (Adapted from [5])

the slow $r^{-\eta}$, $\eta < 0.1$ decay of $g_r(r)$. The melting of the 2D Ce lattice occurs between 9 and 10 K. Between these two temperatures the behavior of $g_r(r)$ changes dramatically – the correlation function decays exponentially above the melting temperature.

In order to detect the hexatic phase, the analysis of the bond-angular correlation function $g_6(r)$ extracted for different temperatures and shown in Fig. 4b is required. In qualitative agreement with the results deduced from the experimental data, surprisingly $g_6(r)$ does not decay to zero at any temperature. In fact, these observations are in complete agreement with the predictions of Nelson and Halperin [30]: for the melting of a 2D crystal on a 'fine mesh' potential, (i) the existence of the hexatic phase is hindered and melting directly occurs from the solid into the liquid phase, (ii) in the liquid phase $g_6(r)$ tends to a finite value at large $r$ and a substrate-induced hexagonal symmetry is present. According to the classification described by Nelson and Halperin [30], the superlattice of Ce/Cu(111) is (i) a commensurate solid at 7 K ($g_r(r) \sim r^{-\eta}$, $\eta = 0$), (ii) a floating solid at 9 K ($g_r(r) \sim r^{-\eta}$, $\eta = 0.09$), (iii) a fluid for $T \geq 10$ K.

For a Ce superlattice on Ag(111), a corresponding theoretical analysis has been performed in which the melting point $T_m$ has been found to be between 4.5 K and 4.9 K [5]. The superlattice of Ce on Ag(111) constitutes a floating solid at 4.0 K ($\eta = 0.14$) and 4.5 K ($\eta = 0.18$), and becomes a fluid for $T \geq 4.9$ K. These findings demonstrate that the behavior of $g_6(r)$ is intrinsic to the Ce/Cu(111) and Ce/Ag(111) superlattices, i. e. the absence of hexatic phase is due to the substrate potential.

The critical parameters defining the surface potential are (i) the adatom diffusion barrier $E_{\text{diff}}$ and (ii) the periodicity, i. e. the separation between nearest adatoms in a superlattice $d$ with respect to the mesh density $r_0$. For Ce on Cu(111) the ratio between $d = 1.3$ nm and $r_0 = 0.256$ nm sets the relative mesh density to $\approx 5$. For Ce on Ag(111) the ratio is $\approx 11$. In both cases, even in the liquid phase the Ce adatoms occupy discrete positions with respect to each other, and only a limited number of angles between two bonds are possible. Consequently, $g_6(r)$ doesn't decay to zero. In the limit of vanishing relative distance between neighboring adsorption sites (i. e. $d/r_0 \gg 1$), hexatic phase appears.

On the other hand, the diffusion barrier height $E_{\text{diff}}$ describes the 'flatness' of the surface. The comparison between $E_{\text{diff}}$ and the thermal energy of the adatom $k_B T$ has to be considered. For $E_{\text{diff}} < k_B T$, the adatom is not influenced by the substrate periodic potential, leading to diffusion on a flat surface: the adatom can be found at any point of the surface and not only in the hollow (adsorption) sites. Thus, at a typical temperature of $T = 10$ K, with $k_B = 0.086$ meV/K, the condition for the appearance of the hexatic phase corresponds to $E_{\text{diff}} < 1$ meV. However, as diffusion barriers $E_{\text{diff}} < 1$ meV have not been observed, the hexatic phase does not exist in the considered class of 2D adatom superlattices.

As a final remark we note that the creation of such adatom superlattices with magnetic adatoms, depending on the relative strength of Kondo scattering versus RKKY interaction, may lead to the formation of ferromagnetic or antiferromagnetic adatom pairs at different separations [33]. Such a 2D superlattice may be of interest

for electron-spin based quantum computing. The ability to control the long range order of magnetic adatoms opens new possibilities and presents new challenges for the investigation of 2D magnetism and for the development of novel atomic-scale magnetic devices.

### *3.3 Reduction of the Superconducting Gap of Ultrathin Pb Islands Grown On Si(111)*

The fundamental question of how the superconducting properties of a material are modified when its thickness is reduced down to a few atomic monolayers, has stimulated considerable theoretical and experimental interest since the 1960's [34–40]. Today, with the emergence of nanoscience and nanotechnology this question is of special relevance for possible technological applications in superconducting nanodevices. The early model of Blatt and Thompson predicted an increase of the critical temperature ($T_c$) above the bulk value with decreasing film thickness, together with $T_c$ oscillations due to quantum size effects (QSE) [34]. However, if proper boundary conditions allowing for spill-out of the electronic wave functions in thin films are taken into account, a decreasing $T_c$ with decreasing film thickness was predicted [37, 38, 41–44]. Depending on the material, early experimental results showed either a decrease (Pb) or an increase (Al, Ga, Sn, In) in $T_c$ on film thickness reduction [45, 46], mainly related to disorder in the films composed of small metallic grains [46]. In contrast, pioneering experiments on crystalline Al films reported no $T_c$ enhancement, allowing to address intrinsic thickness-dependent properties of crystalline superconducting films [47].

Recently, Pb films grown on Si(111) attracted much attention in this context [16]. Ex situ resistivity [48] and magnetic susceptibility measurements [49] reported a decrease of $T_c$ with decreasing Pb film thickness. In contrast, recent in situ scanning tunneling spectroscopy (STS) investigations on Pb/Si(111) islands reported no significant change in $T_c$ upon thickness reduction [50, 51], while the very small $T_c$ oscillations observed were attributed to QSE [34, 50]. These contradictory experimental results call for a clarification.

Recently, we reported in situ layer-dependent STS measurements of the energy gap of ultrahigh-vacuum grown single-crystal Pb/Si(111)-7×7 and Pb-$\sqrt{3} \times \sqrt{3}$/Si(111) islands in the thickness range of 5 to 60 monolayers (ML). In contrast to previous STS studies on this system [50, 51], we show that the energy gap decreases with decreasing island thickness $d$ for both, crystalline and disordered interfaces [6]. Corresponding $T_c$ values, estimated using the bulk gap-to-$T_c$ ratio, decrease with a $-1/d$ dependence, in quantitative agreement with ex situ measurements of Ozer et al. [49].

Figure 5 shows an STM image of a flat-top Pb island extending over two Si terraces separated by a single Si(111) step [52]. The island mainly consists of an 8 ML thick Pb area with respect to the Si surface, as determined from the apparent height in the STM topograph [7]. The inset shows a magnified view of the Pb surface lattice with atomic resolution. The observed superstructure, reflects the buried 7×7

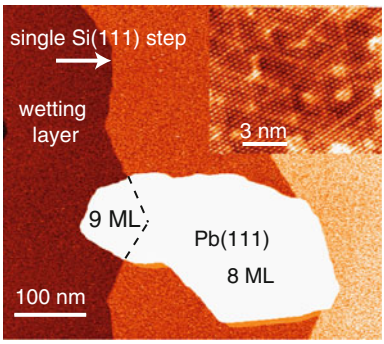


**Fig. 5** (*Color online*). STM image of a flat-top Pb(111) single-crystal island grown on Si(111)-7×7. The island extends over two Si terraces. Island thickness includes the wetting layer. $V_{bias} = -1.0$ V, I = 100 pA. The inset shows a magnified view, revealing the Pb lattice with atomic resolution ($V_{bias} = 20$ mV, I = 1 nA). After Ref. [6]

interface [52]. Pb areas of constant thickness with a lateral extension larger than the $T = 0$ K Pb bulk coherence length ($\sim 80$ nm) were selected for this study, excluding transition regions where the island thickness changes.

Figure 6 displays a selected set of measured $dI/dV$ spectra for the indicated island thicknesses at $T = 3.0$ K. Measurements have also been performed at 4.6 K (not shown). Each curve is an average of more than ten individual $dI/dV$ spectra taken at various locations on one island. The background conductance was subtracted and the curves were normalized. The spectra display a clear superconducting energy gap $\Delta$ decreasing with decreasing island thickness. The observed small spectral asymmetry between positive and negative bias reflects the limits of the background subtraction on the 7×7 interface. Two phonon modes (indicated by

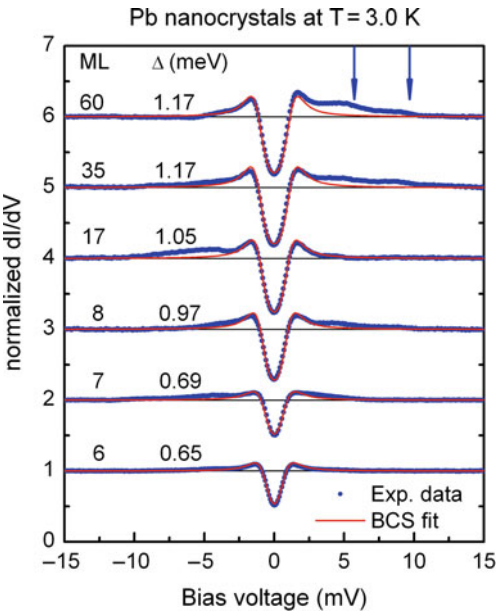


**Fig. 6** (*Color online*). Experimental (*dots*) and calculated (continuous lines) differential conductance spectra for tunneling between a PtIr tip and a large atomically flat Pb island of selected thickness. All spectra are measured at 3.0 K on Pb/Si-7x7, except for the 7ML measured on Pb/Pb-$\sqrt{3} \times \sqrt{3}$/Si. $\Delta_{Bulk}(3.0\ K) = 1.23$ meV. Arrows indicate observed phonon modes. The zero conductance level is indicated for the 6 ML spectrum. The other spectra are vertically displaced for clarity by integers. After Ref. [6]

arrows for the 60 ML curve) are clearly detected. Their energies (the difference between the local extrema in $d^2I/dV^2$ and $\Delta$) are $4.6 \pm 0.2$ meV and $8.5 \pm 0.2$ meV, in excellent agreement with the values reported for bulk Pb [53].

The extracted gap values are averaged and plotted in Fig. 7a as a function of inverse film thickness. The energy gaps for both interfaces show a comparable reduction upon decreasing thickness. To allow for a comparison with previous results, the critical temperature $T_c$ was estimated from the measured gap values using the bulk $\Delta/T_c$ ratio and assuming the BCS temperature dependence of $\Delta(T)$. The results are displayed in Fig. 7b). The continuous line represents a least squares analysis of the STS data, leading to the relation $T_c(d) = 7.08 \times (1 - d_0/d)$ with $d_0 = 1.88$ ML. Consequently, for $d \leq 2$ ML the superconducting properties of Pb are expected to vanish.

Our estimated $T_c$'s are in quantitative agreement with the ones of Ozer et al. [49], obtained ex situ on Ge capped Pb/Pb$\sqrt{3}\times\sqrt{3}$/Si(111). The trend observed in in situ resistivity measurements [54] is consistent with the present findings, the quantitative differences with respect to our data being most likely caused by the inhomogeneity of the films. Ex situ resistivity measurements [48] on Au capped Pb/Si(111)-7×7 films show a much faster decrease of $T_c$ with decreasing film thickness than in

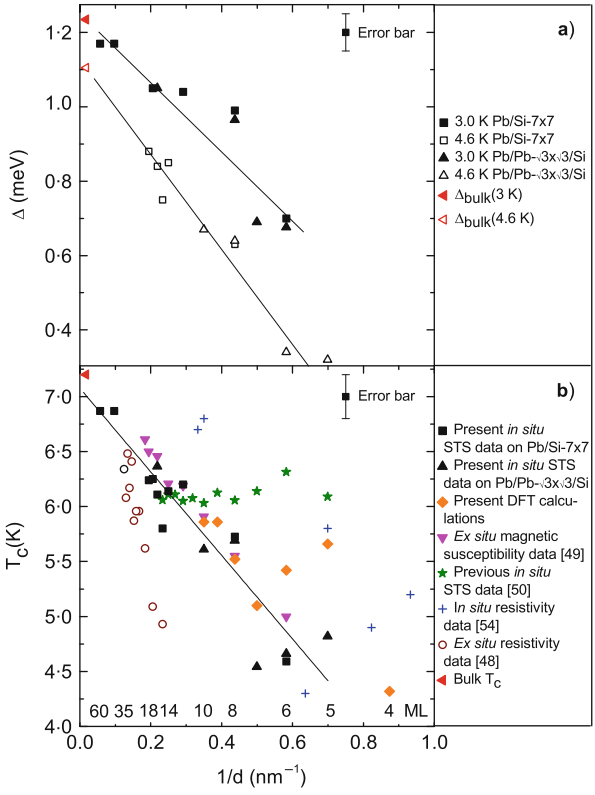


**Fig. 7** (*Color online*). (**a**) Superconducting energy gap $\Delta$ as a function of inverse Pb island thickness $1/d$, extracted from BCS fits of $dI/dV$ tunneling spectra, for the crystalline (Pb/Pb-$\sqrt{3} \times \sqrt{3}$/Si) and disordered (Pb/Si-7×7) interface. Continuous lines are guides for the eyes. b) Estimated critical temperature $T_c$ as a function of $1/d$, using the bulk $\Delta/T_c$ ratio and assuming BCS temperature dependence of $\Delta(T)$, to allow comparison with previously reported results. Continuous line is a fit to the present STS data. For both (**a**) and (**b**) error bars: experimental dispersion and uncertainty in the fit results. After Ref. [6]

our case, probably a consequence of the inverse proximity effect induced in the Pb film by the Au capping layer [55]. However the previous in situ STS results on Pb/Si(111)-7×7, which reported an essentially constant $T_c$ in this thickness range [50, 51], are at variance with our data. Furthermore, our observed energy gap reduction is much larger in amplitude than the very small oscillations of $T_c$ as a function of thickness [50], the amplitude of which is of only 2% of the average $T_c$.

For thin Pb islands on Si(111) the experimentally observed reduction of the superconducting energy gap with decreasing film thickness is consistent with the first principle results of a thickness-dependent electron-phonon coupling constant λ, where close to the ultrathin Pb film limit the variations of the density of states at $E_F$ play a decisive role. Interestingly, both atomically smooth (Pb/Pb-$\sqrt{3} \times \sqrt{3}$/Si) and disordered (Pb/Si-7×7) interfaces yield similar experimental behavior, in agreement with results showing that both systems are in the diffusive limit [49, 56].

### *3.4 Chiral Self-Assembly of Rubrene Molecules on Au(111)*

Surface nanostructuring by molecular self-organization is a relevant process in the growing field of nanotechnology. Depending on the characteristics of the molecules and on the type of interactions among them and with the substrate, a variety of surface patterns have been observed by means of scanning tunneling microscopy (STM) [57]. The aromatic hydrocarbon rubrene (5,6,11, 12-Tetraphenylnaphthacene, $C_{48}H_{28}$) is chiral and non-planar due to intramolecular steric hindrance [58, 59] which causes a twisting of the central tetracene-backbone around its axis and forces the four phenyl-groups to rotate around their $\pi$-bonds. Its highly efficient luminescence established the success of rubrene as a dopant for organic light emitting diodes to improve the efficiency and stability of the devices [60]. Despite this growing interest in the application of rubrene, there have been no nanoscale investigations of the self-assembly process and the molecular and supramolecular chirality of rubrene until recently [8].

Figure 8 shows the surprising hierarchical complexity of the nested 2D supramolecular assembly of rubrene on gold with its three successive generations: single molecules, pentagonal supermolecules and supramolecular decagons. The chirality of the individual molecules is conserved in both assembly-steps. Due to the chirality dependent rotation of the building blocks, both resulting generations of the progression are chiral on their own. Since this self-organization of increasing complexity is enantioselective on the molecular and supramolecular level, we obtain a spontaneous resolution of the original racemic mixture of individual molecules into homochiral architectures. Our findings on the conservation and recognition of chirality on all stages of the supramolecular self-assembly of rubrene may have an impact on the development of chiral molecular electronic and optoelectronic devices and exemplify the working principle of basic processes in nature.

A very interesting aspect in this context is the 3D chirality transfer in rubrene multilayer islands [11]. Multilayer islands up to a thickness of six layers on a Au(111) surface have been investigated. The molecules self-organize in parallel

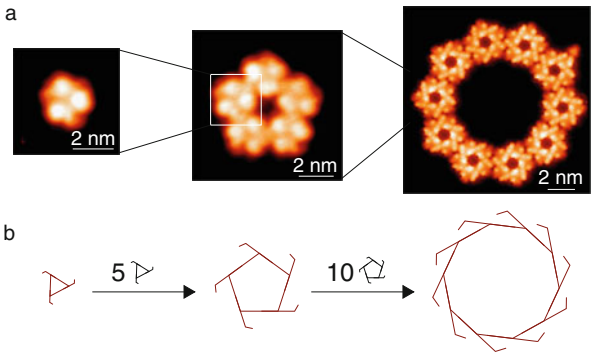


**Fig. 8** Hierarchy and conservation of chirality in the spontaneous 2D supramolecular assembly. a, STM images representing the three generations of the nested two-staged self-organization. From left to right: single molecule, pentagonal supermolecule, supramolecular decagon. Typical tunneling parameters are I = 20 pA and V = −0.8 V. b, From left to right: Enantioselective assembly from L-type monomers to L-type pentagons and further on to L-type decagons. After Ref. [8]

twin rows, forming mirror domains of defined local structural chirality. Each layer is composed of twin-row domains of the same structural handedness rotated by 120° with respect to each other. Moreover, this structural chirality is transferred to all successive layers in the island, resulting in the formation of 3D objects having a defined structural chirality. The centered rectangular surface unit cell differs from the one characteristic for the single-crystal orthorhombic phase.

Two-dimensional (2D) tiling constitutes a fundamental issue in topology [61], with fascinating examples in nature and art, and applications in many domains such as cellular biology, [62], foam physics [63], or crystal growth [64]. Recently, we presented the first observation of surface tiling with both, non-periodic and periodic arrangements of slightly distorted pentagons, hexagons, and heptagons formed by rubrene molecules adsorbed on a Au(111) surface [10]. On adjacent regions of the sample, ordered honeycomb and hexagonal close-packed patterns are found. The existence of manifold arrangements in the supramolecular self-assembly of rubrene on gold originates from the 3D non-planar flexible structure of the molecule, as well as from the nature of the intermolecular bonds.

A detail of the latter non-periodic phase is shown in Fig. 9a. The dashed blue circle surrounds a single rubrene molecule, with the sub-molecular contrast revealing three lobes and a quite regular three-fold symmetry [8, 9]. The self-assembled pattern is composed of supramolecular pentagons, hexagons and filled heptagons, which appear to be randomly distributed over the surface. There exist 11 distinct tilings by regular polygons [61], however, a combination of regular pentagons, hexagons, and heptagons generates empty gaps and overlapping regions, as inferred from the consideration of the angles at the corners of a regular pentagon (108°), hexagon (120°) and heptagon ($\approx$ 129°). Only in the case of joining three hexagons with one common corner, the angular sum is exactly 360°. Nevertheless, there exist three configurations yielding an angular sum close to 360°, schematized in Fig. 9b: